

1 **Analytical assessment of Kelvin-Helmholtz instability growth at Ganymede's upstream**
2 **magnetopause**

3

4 *N. Kaweeyanun(1), A. Masters(1), X. Jia(2)

5

6 (1) Department of Physics, Imperial College London

7 (2) The Climate and Space Sciences and Engineering Department, University of Michigan

8

9 Corresponding author: N. Kaweeyanun

10 Corresponding author email: nk2814@ic.ac.uk

11

12 **Key Points**

- 13 • We present the first assessment of Kelvin-Helmholtz (K-H) instability on
14 Ganymede's upstream magnetopause using an analytical model.
- 15 • Linear K-H waves can grow on both magnetopause flanks with small enhancement on
16 the sub-Jovian flank due to the finite Larmor radius effect.
- 17 • Nonlinear K-H vortices should be suppressed by magnetic reconnection, so the latter
18 likely dominates cross-magnetopause plasma transport.

19

20 **Abstract**

21 Ganymede is the only Solar System moon that generates a permanent magnetic field.
22 Dynamics within the Ganymede magnetosphere is thought to be driven by energy-transfer
23 interactions on its upstream magnetopause. Previously in Kaweeyanun et al. (2020), we

24 created a steady-state analytical model of Ganymede's magnetopause and predicted global-
25 scale magnetic reconnection to occur frequently throughout the surface. This paper
26 subsequently provides the first assessment of Kelvin-Helmholtz (K-H) instability growth on
27 the magnetopause. Using the same analytical model, we find that linear K-H waves are
28 expected on both Ganymedean magnetopause flanks. Once formed, the waves propagate
29 downstream at roughly half the speed of the external Jovian plasma flow. The Ganymedean
30 K-H instability growth is asymmetric between magnetopause flanks due to the finite Larmor
31 radius (FLR) effect arising from large gyroradii of Jovian plasma ions. A small but notable
32 enhancement is expected on the sub-Jovian flank according to the physical understanding of
33 bulk plasma and local ion flows alongside comparisons to the well-observed magnetopause
34 of Mercury. Further evaluation shows that nonlinear K-H vortices should be strongly
35 suppressed by concurring global-scale magnetic reconnection at Ganymede. Reconnection is
36 therefore the dominant cross-magnetopause energy-transfer mechanism and driver of global-
37 scale plasma convection within Ganymede's magnetosphere.

38

39

40 **Plain Language Summary**

41 Ganymede is the largest moon of Jupiter, and the only moon in the Solar System that can
42 maintain a permanent magnetic field. Current research suggests Ganymede contains two
43 internal magnetic field sources – a molten iron core and a subsurface ocean. The study of
44 Ganymede's magnetic environment will be a primary objective for the JUpiter ICy moon
45 Explorer (JUICE), the first moon-orbiting satellite mission set to launch in 2022. Ganymede
46 is surrounded by flows of plasma (energized gas) which are normally deflected away by the
47 magnetic field along a boundary called the upstream magnetopause. However, the magnetic
48 shield can be broken through interactions on the magnetopause such as Kelvin-Helmholtz (K-

49 H) instability. Using a mathematical model established in Kaweeyanun et al., (2020), we first
50 determine that K-H instability can grow as waves along Ganymede's magnetopause flank
51 regions, and that the growth is enhanced on the magnetopause flank that is closest to Jupiter
52 due to motions of local plasma. Finally, using Mercury as a comparison case, we argue that
53 K-H waves are unlikely to grow into turbulent vortices that can inject plasma across the
54 magnetopause, as they will be torn apart by another magnetopause process known as
55 magnetic reconnection.

56

57 **Key Words**

58 Ganymede, Kelvin-Helmholtz instability, analytical model, finite Larmor radius effect,
59 magnetic reconnection

60

61 **1. Introduction**

62 Between 1996-2000, the Galileo spacecraft performed six flybys of Ganymede, the largest
63 moon of Jupiter and the Solar System, during which evidence of a permanent magnetic field
64 was detected (Kivelson et al., 1996; Gurnett et al., 1996). Ganymede's equatorial surface
65 magnetic field is ~ 7 times stronger than the ambient Jovian magnetic field, allowing
66 Ganymede to maintain a small distinct magnetosphere inside Jupiter's much larger one
67 (Kivelson et al., 1998; Kivelson et al., 2002). The primary source of Ganymede's magnetic
68 field is thought to be dynamo action inside an Earth-like molten iron core (Anderson et al.,
69 1996; Schubert et al., 1996). The magnetic field is close to dipolar with a $\sim 176^\circ$ tilt between
70 the magnetic and rotation axes, but the angle varies by a few degrees between Galileo flybys
71 (Kivelson et al., 2002). The dipole tilt variation may be explained by non-negligible higher
72 order (e.g., quadrupole) moments in Ganymede's permanent magnetic field, or more likely a
73 large subsurface ocean whose inductive response generates a secondary induced magnetic

74 field (Kivelson et al., 2002). This potential water presence makes Ganymede the primary
75 destination for the upcoming JUPITER ICY moon Explorer (JUICE) space mission (Grasset et
76 al., 2013).

77

78 The Jovian magnetosphere around Ganymede is significantly populated by plasma released
79 from Io's volcanoes. The plasma diffuses outward over time, while rotating in the same
80 direction as Jupiter's rotation, to form a $\sim 3 R_J$ ($R_J = 71,492$ km) thick plasma sheet centered
81 around the Jovian centrifugal equator (Kivelson et al., 2004). This plane is tilted $\sim 7^\circ$ with
82 respect to Ganymede's orbit, which lies close to Jupiter's geographical equator, so the moon
83 experiences large variations in plasma and magnetic conditions as it moves up and down
84 through the plasma sheet (Kivelson et al., 2004). At Ganymede's average orbital distance of
85 $15 R_J$, the Jovian plasma consists primarily of heavy oxygen and sulfur ions with only 10%
86 contribution from protons – a sharp contrast from the proton-dominated solar wind (Bagenal
87 et al., 2016). Furthermore, the Jovian plasma flow speed near Ganymede is sub-Alfvénic (i.e.,
88 magnetic pressure dominant) which leads to a cylindrical magnetosphere (Neubauer, 1998),
89 unlike the super-Alfvénic (i.e., dynamic pressure dominant) solar wind that creates bullet-
90 shaped planetary magnetospheres (Neubauer, 1990). The environment around Ganymede
91 hence provides a unique laboratory to study plasma and magnetic interactions in the Solar
92 System.

93

94 Based on the magnetic topology, Ganymede's magnetosphere can be divided into “open-
95 field” and “closed-field” regions. The open-field region covers Ganymede's polar caps and
96 most of the magnetotail. In this region, each magnetic field line connects from one of
97 Ganymede's magnetic poles to the corresponding Jupiter's magnetic poles, forming an
98 extended magnetotail structure known as the Alfvén wings (Neubauer, 1998; Jia, Kivelson et

99 al., 2010). Under the ideal magnetohydrodynamic (MHD) theory, plasma particles can enter
100 and escape Ganymede's magnetosphere along these open field lines, but they do not have
101 sufficiently large number or velocity to influence dynamics inside the magnetosphere (Frank
102 et al., 1997; Williams, Mauk, & McEntire, 1997; Williams, Mauk, McEntire, Roelof et al.,
103 1997). Meanwhile, the closed-field region spans the low-latitude areas upstream and
104 downstream of Ganymede, in which each magnetic field line has both ends connected to the
105 moon. On the upstream side, the outermost closed magnetic field lines are compressed by the
106 ambient Jovian plasma flow along a boundary known as the upstream magnetopause.
107 Dynamics inside Ganymede's magnetosphere are likely driven by interactions on the
108 upstream magnetopause, similar to a Dungey cycle in planetary magnetospheres (e.g., Jia,
109 Walker et al., 2010; Collinson et al., 2018). Two of the most commonly studied
110 magnetopause interactions are magnetic reconnection and Kelvin-Helmholtz (K-H)
111 instability. We have previously investigated global magnetic reconnection at Ganymede's
112 upstream magnetopause in Kaweeyanun et al. (2020), therefore this paper will focus on the
113 role of K-H instability in energy transport into Ganymede's magnetosphere.

114

115 K-H instability arises from bulk flow shear between plasmas just outside and inside a
116 magnetopause boundary. The instability can be divided into two distinct phases – a linear
117 phase in which the magnetopause develops wavelike oscillations (e.g., Dungey, 1955;
118 Southwood, 1968), followed by a nonlinear phase in which the waves grow into turbulent
119 vortices (e.g., Southwood, 1979; Miura, 1982). The nonlinear phase is particularly important
120 as multiple plasma/magnetic layers become tightly wound inside a K-H vortex, separated by
121 very thin and unstable current sheets. These conditions can facilitate cross-magnetopause
122 energy transport via turbulent decay (Nakamura et al., 2004; Matsumoto & Hoshino, 2006),
123 coupling with kinetic Alfvén waves (Chaston et al., 2007), or inducing magnetic reconnection

124 within the vortex (Nykyri & Otto, 2001; Nakamura et al., 2008). The existence of linear K-H
125 waves at Ganymede's upstream magnetopause has been speculated from Galileo observations
126 (Kivelson et al., 1998; Volwerk et al., 1999; Volwerk et al., 2013) and a numerical model
127 (Tóth et al., 2016). However, there has not been a focused study on K-H vortices, or general
128 K-H instability growth, on Ganymede's magnetopause.

129

130 The assessment detailed in this paper thus relies on K-H instability knowledge gained from
131 previous planetary magnetopause studies. Both K-H waves and vortices have been observed
132 at Earth's magnetopause, with evidence of energy transport in the vortex phase (Fairfield et
133 al., 2000; Owen et al., 2004; Hasegawa, Fujimoto, Phan et al., 2004). Similar detections of
134 two K-H instability phases are seen at Saturn's magnetopause (Masters et al., 2009; Masters
135 et al., 2010; Wilson et al., 2012; Delamere et al., 2013), and the instability is predicted for
136 Jupiter's magnetopause (Desroche 2012; Masters 2017; Zhang et al., 2018). Magnetic guide
137 field component along the plasma flow shear is found to stabilize K-H instability growth,
138 therefore K-H vortices are expected mainly on magnetopause flanks where magnetosheath
139 and magnetospheric magnetic fields are either parallel or antiparallel (Thomas and Winske,
140 1993; Miura, 1995; Eastwood et al., 2015). Observations suggest K-H vortices strongly favor
141 the parallel magnetic configuration i.e., when the interplanetary magnetic field (IMF) is
142 northward for Earth (Hasegawa, Fujimoto, Phan et al., 2004) and southward for Saturn
143 (Masters et al., 2010), but smaller intermittent instability growth is viable under the
144 antiparallel configuration i.e., when the IMF is southward for Earth (Hwang et al., 2011; Yan
145 et al., 2014; Kavosi & Raeder, 2015). The latter scenario is particularly important because
146 Ganymede's magnetopause always maintains a near-antiparallel magnetic configuration due
147 to the moon's 176° magnetic axis tilt angle and the dominant southward component of the
148 Jovian magnetic field.

149

150 There is a temptation to assess K-H instability assessment only through the ideal MHD
151 theory. However, observations from Mercury's magnetopause indicate that kinetic effects can
152 also play an important role in K-H instability growth. Both K-H linear waves and nonlinear
153 vortices have been observed at Mercury's magnetopause by the MErcury Surface, Space,
154 ENvironment, Geometry, and Ranging (MESSENGER) spacecraft (Slavin et al., 2008;
155 Boardson et al., 2010; Sundberg et al., 2012; Liljeblad et al., 2014). But unlike other
156 planetary cases, K-H vortices are seen almost exclusively on the dusk magnetopause flank
157 (Sundberg et al., 2012; Liljeblad et al., 2014). The asymmetry can be explained by the finite
158 Larmor radius (FLR) effect, a kinetic phenomenon arising when local plasma ion gyroradii
159 are significant compared to the magnetopause thickness. The FLR effect has been studied
160 analytically through small mathematical corrections to the ideal MHD theory (Nagano, 1978;
161 Nagano, 1979; Huba, 1996; Glassmeier & Espley, 2006; Sundberg et al., 2010), and
162 numerically through kinetic simulations (e.g., Nakamura et al., 2010; Paral & Rankin, 2013).
163 Given that Ganymede also has a thin magnetopause (<400 km from Kivelson et al., 1998)
164 and is surrounded by heavy Jovian plasma ions with large gyroradii, the FLR effect must be
165 considered when evaluating K-H instability growth around the moon.

166

167 In this paper, we begin with an assessment of the K-H instability onset at global scale under
168 the ideal MHD theory, and the subsequent propagation of linear K-H waves (Section 2).
169 Then, we present a schematic picture of the FLR effect, and evaluate its strength on
170 Ganymede's magnetopause flanks using Mercury as an analogue (Section 3). Lastly, we
171 determine the potential for nonlinear K-H vortex growth and whether K-H instability
172 significantly contributes to energy transport across Ganymede's magnetopause (Section 4).

173

174 2. Assessment of K-H Instability Onset across Ganymede's Upstream 175 Magnetopause

176 The K-H instability onset assessment utilizes an analytical model which parametrizes steady-
177 state plasma and magnetic conditions on both sides of an idealized Ganymedeian
178 magnetopause surface (Kaweeyanun et al., 2020). The model considers an infinitesimally
179 thin magnetopause with magnetized adjacent plasma and assumes there are no competing
180 interactions, such as global-scale magnetic reconnection, during the K-H instability growth.
181 This is a highly idealized situation designed to study the operation of key physics at minimal
182 computational cost.

183

184 The model operates in a Cartesian coordinate system centered at Ganymede (GphiO) where
185 X is parallel to the ambient Jovian plasma flow, Y points toward Jupiter, and Z points
186 approximately toward Ganymede's geographical north pole. The simulation domain is
187 $-4.0 < Y < 4.0 R_G$ and $-1.0 < Z < 1.0 R_G$ with $0.01 R_G$ resolution in each dimension. The
188 model accounts for Ganymede's up-down movement in the Jovian plasma sheet via Jupiter's
189 east longitude parameter ϕ . The magnetopause is north-south symmetric when Ganymede
190 lies at the center of the Jovian plasma sheet ($\phi = 248^\circ$) and gains largest asymmetry when
191 the moon reaches its highest point ($\phi = 158^\circ$) and lowest point ($\phi = 338^\circ$) in the plasma
192 sheet. We will consider these three specific cases when evaluating the K-H instability onset
193 condition.

194

195 Figure 1, adapted from Kaweeyanun et al. (2020), demonstrates the parametrizations of
196 plasma and magnetic parameters for the case when $\phi = 248^\circ$. The magnetopause is first

197 projected onto a Y-Z plane (with the Jovian plasma flowing into page) and the surface X-
198 coordinates shown in Figure 1a. As expected, the magnetopause curves downstream (X value
199 increasing) toward the flanks. The red dots indicate equatorial flank points ($X = 0, Z = 0$)
200 where magnetic field strengths will be used to calculate ion gyromotion properties in Section
201 3.

202

203 The ambient Jovian plasma is assumed to flow at $v_{J,0} \approx 140$ km/s along the X-direction for
204 all Ganymede positions (Jia et al., 2008). Figure 1b depicts plasma bulk flow velocity (\mathbf{v}_J)
205 on the Jovian-side magnetopause for $\phi = 248^\circ$. The flow collides with the magnetopause
206 and the Jovian-side speed (v_J) is parametrized as a sine function of the flaring angle between
207 the local magnetopause normal and the ambient flow direction (Kaweeyanun et al., 2020).
208 Hence, the flow speed is slowest near the subflow point ($Y = 0, Z = 0$) where the collision is
209 head-on, and increases along the flanks where the flow is less impeded by the magnetopause.
210 Normalized arrows indicate Jovian-side flow directions consistent with plasma traversing
211 around Ganymede along the magnetopause surface (Kaweeyanun et al., 2020).

212

213 The ambient Jovian plasma mass density depends on Ganymede's position in the plasma
214 sheet, maximized at $\rho_{J,0} = 56$ amu/cm³ when $\phi = 248^\circ$ and minimized at $\rho_{J,0} = 28$
215 amu/cm³ when $\phi = 158^\circ, 338^\circ$ (Kivelson et al., 2004; Jia et al., 2008). Figure 1c shows the
216 Jovian-side mass density (ρ_J) when $\phi = 248^\circ$. The Jovian-side mass density is parametrized
217 as a cosine function of the flaring angle with a positive offset equal to the ambient density, as
218 the plasma gains density from magnetopause collision (Kaweeyanun et al., 2020). The

219 density is highest near the subflow point where head-on collision creates largest plasma
220 compression, and lowest near the flanks where the compression is negligible.

221

222 The combined thermal plasma and energetic particle pressure of the ambient Jovian plasma is
223 $P_{J,0} = 3.8$ nPa when $\phi = 248^\circ$ and $P_{J,0} = 1.9$ nPa when $\phi = 158^\circ, 338^\circ$ (Kivelson et al.
224 2004; Jia et al., 2008). Figure 1d shows the Jovian-side pressure (P_J) when $\phi = 248^\circ$. Like
225 the mass density, the pressure increase from near-magnetopause compression is parametrized
226 as a cosine relation of the flaring angle and added to the ambient values, resulting in higher
227 pressure near the subflow point and lower pressure along the flanks (Kaweeyanun et al.,
228 2020).

229

230 In our model, the ambient magnetic field carried by the Jovian plasma has strength $B_{J,0} = 70$
231 nT when $\phi = 248^\circ$ and $B_{J,0} = 105$ nT when $\phi = 158^\circ, 338^\circ$ (Khurana, 1997; Jia et al.,
232 2008). Assuming negligible $B_{J,0,x}$ component (Jia et al., 2008), the ambient Jovian field
233 strength is distributed between $B_{J,0,y}$ and $B_{J,0,z}$ components such that the field points along
234 negative Z -direction when $\phi = 248^\circ$, and deviates $\approx 45^\circ$ from negative Z -direction when
235 $\phi = 158^\circ, 338^\circ$ (Jia et al., 2008; Kaweeyanun et al., 2020). The magnetic field is compressed
236 near the magnetopause similar to the mass density and pressure, so the Jovian-side field (\mathbf{B}_J)
237 is strongest near the subflow point and weakest along the flanks as shown in Figure 1e when
238 $\phi = 248^\circ$. The magnetic field strength is $B_J \approx 67$ nT at both equatorial flank points. The
239 pressure conservation method used to determine the Jovian-side field strength is previously
240 discussed in Kaweeyanun et al., (2020). The Jovian-side field direction (normalized arrows)

241 is similar to the ambient direction, but additionally constrained to be parallel to the
242 magnetopause surface (Kaweeyanun et al., 2020).

243

244 Plasma inside Ganymede's magnetosphere exerts negligible pressure due to its relatively cold
245 temperature (Jia et al., 2008). Therefore, Ganymede's magnetic field solely produces the
246 balancing pressure against the Jovian-side plasma and magnetic pressures combined. This
247 allows computation of the Ganymede-side magnetic field (\mathbf{B}_G) shown in Figure 1f when
248 $\phi = 248^\circ$. As expected, the Ganymede-side field strength is strongest near the subflow
249 point and weakest along the flanks. The magnetic field strength is $B_G \approx 122$ nT at both
250 equatorial flank points, which is in general consistent with the Galileo observations during
251 magnetopause crossings (Kivelson et al., 1998). The field direction (normalized arrows) is
252 required to be approximately dipolar and parallel to the magnetopause (Kaweeyanun et al.,
253 2020). The magnetic field points northward in the closed-field region and southward in the
254 open-field region. The Ganymede-side mass density and bulk plasma flow speed are taken
255 to be uniform with magnitudes $\rho_G = 32$ amu/cm³ and $v_G = 0$ km/s respectively.

256

257 Once we obtain the magnetopause conditions exemplified in Figure 1 for all three Ganymede
258 positions, the K-H instability onset condition is evaluated in the closed-field region where the
259 instability can potentially influence Ganymede's magnetospheric dynamics. Linear K-H
260 instability waves can form on Ganymede's magnetopause if adjacent plasma and magnetic
261 conditions satisfy the following inequality (Farrugia et al., 1998; Masters, 2017)

$$[\mathbf{k} \cdot (\mathbf{v}_J - \mathbf{v}_G)]^2 > \frac{1}{\mu_0} \left(\frac{1}{\rho_J} + \frac{1}{\rho_G} \right) [(\mathbf{k} \cdot \mathbf{B}_J)^2 + (\mathbf{k} \cdot \mathbf{B}_G)^2] \quad \#(1)$$

262 where \mathbf{k} is the K-H wavevector of unit length, \mathbf{v} is bulk flow velocity vector, \mathbf{B} is magnetic
263 field vector, r is plasma mass density, and $\mu_0 = 4\pi \times 10^{-7}$ H/m is the vacuum permeability
264 constant. Subscripts “J” and “G” denote Jovian and Ganymedean sides of the magnetopause
265 respectively.

266

267 At each magnetopause surface point, we first assess the onset condition with the K-H
268 wavevector parallel to the bulk flow shear (subsequently defined as $\mathbf{v}_{\text{sh}} = \mathbf{v}_J - \mathbf{v}_G$), and then
269 reassess the condition after every 1° wavevector rotation. Two criteria are required for a point
270 to be considered “K-H unstable”. First, the point must have at least one wavevector
271 orientation that satisfies the onset inequality. Second, the point must have at least four
272 neighboring points that satisfy the first criterion. The latter criterion removes the “isolated
273 unstable points” (i.e., inequality satisfied by a smallest margin for only one wavevector
274 orientation) where the K-H instability effectively cannot grow. From equation (1), the K-H
275 unstable condition is favored if 1) the bulk flow shear is large, 2) mass densities on both sides
276 of the boundary are large, 3) adjacent magnetic fields are weak, and 4) the K-H wavevector is
277 parallel to the bulk flow shear and/or orthogonal to adjacent magnetic fields.

278

279 At each K-H unstable point, we calculate the zero-momentum (center-of-mass) frame
280 velocity along which the K-H linear wave propagates following

$$\mathbf{v}_p = \left(\frac{\rho_J}{\rho_J + \rho_G} \right) \mathbf{v}_J \# (2)$$

281 where the parameters retain their usual definitions. Since we consider one cross-
282 magnetopause volume containing both Jovian-side and Ganymedean-side plasmas, mass

283 densities can substitute for masses in the velocity expression. The equation indicates that K-H
284 waves always propagate in same direction as the external Jovian-side bulk flow.

285

286 Figure 2 shows the K-H instability onset condition assessment in the closed-field region for
287 (a) $\phi = 248^\circ$, (b) $\phi = 158^\circ$, and (c) $\phi = 338^\circ$. Magnetopause conditions are K-H unstable
288 in the colored regions and K-H stable in the white regions. The color scale and normalized
289 arrows describe zero-momentum frame speed and direction respectively. Figure 2a indicates
290 that when Ganymede lies at the center of Jovian plasma sheet, its magnetopause is almost
291 entirely K-H unstable except for the areas immediately north/south of the subflow point. The
292 zero-momentum frame speed ranges from <1 km/s closest to the subflow point up to 89 km/s
293 far along the magnetopause flanks. Figures 2b-2c show sizable reductions in K-H unstable
294 areas as Ganymede is at highest and lowest points relative to the plasma sheet's center. K-H
295 waves can form only inside narrow strips along magnetopause flanks beyond $|Y| > 2 R_G$.
296 The zero-momentum frame speed has a smaller range of 50-66 km/s at these Ganymede
297 positions. We see that the K-H waves can still propagate toward the magnetopause flanks, but
298 with evident effects from the north-south magnetopause asymmetry.

299

300 There are two factors why Ganymede's magnetopause become less K-H unstable when
301 $\phi = 158^\circ, 338^\circ$. First, adjacent magnetic fields are 50% stronger compared to when $\phi =$
302 248° , while Jovian-side mass densities are 50% less dense. Both parameter changes increase
303 the threshold for K-H instability onset (right-hand side of the inequality). The K-H unstable
304 area size is much more sensitive to magnetic field strengths than mass densities as the onset
305 threshold is proportional to $|B_J|^2$ and $\frac{1}{\rho_J}$ respectively. Second, the north-south magnetopause

306 asymmetry means the bulk flow shear becomes more parallel to the adjacent magnetic fields
307 at $|Y| < 2 R_G$. Therefore, the field-orthogonal K-H wavevector that minimizes the threshold
308 still may not sufficiently raise the left-hand side of the inequality to satisfy the onset
309 condition as the wavevector is also not parallel to the bulk flow shear. Sensitivity tests
310 suggest that both factors have significant impacts on K-H instability onset, but a quantitative
311 impact comparison is difficult as our analytical model only provides estimative results.

312

313 The K-H instability onset is impacted not only by Ganymede's spatial position, but also
314 temporal changes in the Jovian plasma sheet. Although the analytical model assumes steady-
315 state conditions, temporal effects can be mimicked by changing plasma parameters without
316 changing Ganymede's position. Figure 3 illustrates K-H instability onset when the Jovian-
317 side flow speed and mass densities vary by $\pm 50\%$ (magnetic field strengths unchanged due to
318 fixed Ganymede position). The size of K-H unstable area is much more sensitive to the
319 Jovian-side flow speed (Figures 3a-3b) than mass density (Figures 3c-3d), because the left-
320 hand side of the onset condition linearly depends on v_j . But unlike adjacent magnetic fields,
321 increasing the flow speed enlarges K-H unstable areas. Interestingly, the impact of -50% flow
322 speed (Figure 3a) is significantly greater than that of +50% flow speed (Figure 3b). The
323 asymmetry occurs because the bulk flow shear is almost parallel to adjacent magnetic fields
324 directly above/below the subflow point, so the magnetopause is highly K-H stable in these
325 regions.

326

327 When $\phi = 248^\circ$, Figure 2a data shows that K-H linear waves propagate at $v_p \sim 0.65v_{sh}$
328 inside the K-H unstable flank regions. When $\phi = 158^\circ, 338^\circ$, Figures 2b-2c data show the

329 propagation speed is $v_p \sim 0.48v_{sh}$. These values indicate that the assumption $v_p \sim 0.5v_{sh}$
330 often seen in literature (e.g., Kivelson et al., 1998) is generally reasonable.

331

332 **3. Evaluation of the FLR effect on Ganymede's magnetopause flanks**

333

334 Figure 2 shows that Ganymede's magnetopause flanks ($|Y| > 2 R_G$) are generally K-H
335 unstable irrespective of the moon's position in the Jovian plasma sheet. K-H instability
336 growth at Ganymede is impacted by the FLR effect, which is illustrated schematically in
337 Figure 4a. Ganymede's magnetopause flanks are defined as 'sub-Jovian' and 'anti-Jovian',
338 where the former lies between Ganymede and Jupiter. Plasma-magnetic configurations on
339 sub-Jovian and anti-Jovian flanks are similar to those on planetary 'dawn' and 'dusk' flanks
340 respectively. The naming change is due to differing plasma geometry, as the Jovian plasma
341 rotates around Jupiter while the solar wind travels radially away from the Sun.

342

343 Looking from above Ganymede's equatorial plane, the ambient Jovian plasma flows at speed
344 $v_{J,0}$ from top of Figure 4a and is symmetrically deflected by the magnetopause, creating two
345 Jovian-side bulk flows of equal speed v_J along the magnetopause flanks. If we assume flank-
346 symmetric Ganymede-side bulk flow of speed v_G resulting from the global-scale Dungey-
347 type reconnection (e.g., Jia et al., 2009; Jia, Walker et al., 2010), then bulk flow shears
348 $v_{sh} = v_J - v_G$ create equal vorticities (black circular arrows) that point southward (into
349 page) on sub-Jovian flank and northward (out of page) on anti-Jovian flank.

350

351 The zoom windows show local plasma ion gyromotions near the magnetopause flank points
352 ($X = 0, Z = 0$). The adjacent magnetic fields are assumed to be perfectly orthogonal to bulk
353 plasma flows in the equatorial plane, with the Jovian field pointing directly southward (into
354 page) and the Ganymede field pointing directly northward (out of page). This magnetic
355 field configuration is typical near Ganymede's magnetopause, since the Jovian magnetic field
356 never deviates beyond 45° from the Z-axis and Ganymede has a 176° dipole axis tilt
357 (Khurana 1997; Kivelson et al., 1998; Jia et al., 2008). Local plasma ions gyrate around
358 magnetic field lines according to the left-hand rule (colored circular arrows), creating Jovian-
359 side $v_{i,J}$ and Ganymede-side $v_{i,G}$ ion flows. The resulting ion flow shears $v_{i,sh} = v_{i,J} - v_{i,G}$
360 create equal southward vorticities (black circular arrows) on both sub-Jovian and anti-Jovian
361 flanks. The ion vorticity will strengthen (weaken) K-H instability growth if it is parallel
362 (antiparallel) to the bulk vorticity. Hence, Figure 4a predicts enhancement from the FLR
363 effect on the sub-Jovian flank where bulk and ion vorticities are parallel.

364

365 A similar schematic diagram can be drawn for Mercury's dayside magnetopause flanks in
366 Figure 4b. The external interplanetary magnetic field (IMF) is taken to be directly northward
367 (out of page) since K-H instability growth is predominantly observed under this field
368 orientation. In contrast from the Ganymede case, internal magnetospheric ions drive the
369 FLR effect as their gyroradii far exceed those of external magnetosheath ions. The principle
370 of bulk-ion vorticity alignment predicts enhanced K-H instability growth on the Hermean
371 dusk flank, consistent with observations from the MESSENGER spacecraft (Sundberg et al.,
372 2012; Liljeblad et al., 2014).

373

374 In Figure 4, the FLR effect is expected to be more significant when the ion flow shear is
375 larger. Based on this information, it is possible to approximately quantify the FLR effect at
376 Ganymede using Mercury as a reference by comparing the ion flow shears between the two
377 bodies. Local ion flow speed can be derived from ion kinetic energy $v_i = \sqrt{\frac{2k_B T_i}{M_i}}$. In Table 1,
378 we calculate ion flow speeds, and subsequently the shears, near the magnetopause flanks of
379 Ganymede (in case of $\phi = 248^\circ$) and Mercury (at perihelion and aphelion separately due to
380 different solar wind conditions). Both perihelion and aphelion Hermean ion flow shears
381 exceed the Ganymedean counterpart by at least a factor of 10. MESSENGER observations
382 indicate that 93% of K-H instability events seen near Mercury occur on the dusk flank
383 (Liljeblad et al., 2014). If we assume that the inter-flank asymmetry in K-H instability growth
384 is linearly proportional to the ion flow shear, then the difference factor of 10 implies that
385 ~54% of all Ganymedean K-H instability events should be seen on the sub-Jovian flank,
386 which is a small but noticeable enhancement.

387

388 Quantifying the FLR effect directly through the ion flow shear can be questionable given the
389 complex physics governing the phenomenon. Hence, we also consider existing studies of the
390 FLR effect, which utilize either analytical MHD-FLR theory or numerical kinetic simulation
391 (see Section 1). The two methods have produced a significant contradiction when applied at
392 Mercury, in which the MHD-FLR theory predicts K-H instability enhancement on the dawn
393 flank, but the kinetic simulation favors the dusk flank (e.g., Sundberg et al., 2010; Nakamura
394 et al., 2010).

395

396 The mathematical difference between MHD-FLR and kinetic theories likely lies in the energy
397 equation, where the former takes a more simplistic form (Umeda et al., 2016). The two
398 methods explain the cause of asymmetric K-H instability growth differently. Under the
399 MHD-FLR theory, the FLR effect arises from relative directions of linear K-H wave phase
400 velocity and local ion diamagnetic drift, the latter of which differs between magnetopause
401 flanks (Huba, 1996). The linear phase asymmetry is then propagated into nonlinear K-H
402 vortex growth. In contrast, kinetic simulation shows that linear K-H wave growth should be
403 flank symmetric as the magnetopause current sheet rapidly broadens beyond the kinetic scale
404 (Nakamura et al., 2010). However, the FLR effect still manifests during linear-to-nonlinear
405 phase transition due to local ion centrifugal drifts in response to a convective electric field.

406

407 As kinetic simulations are computationally expensive, one might try to apply the analytical
408 MHD-FLR theory to the Ganymede system. Such attempt would be hindered by two
409 unresolved issues. First, the theory requires higher-order gyro-viscosity corrections to be
410 small, but they diverge for an infinitesimally thin magnetopause which is assumed for the
411 analytical theory (Nagano, 1978; Nagano, 1979). Second, the first-order gyro-viscosity tensor
412 is formulated under a coordinate system that assumes parallel adjacent magnetic fields
413 (Nagano, 1978; Nagano, 1979), which is not the case for Ganymede given that the southward
414 Jovian magnetic field creates an anti-parallel magnetic field configuration near the
415 magnetopause.

416

417 Despite its imperfections, the MHD-FLR theory still offers some insights that can help
418 quantify the FLR effect. The asymmetry in K-H instability growth is likely proportional to

419 the sum of gyro-viscous coefficients, which are constant multipliers for the corrective tensor,
420 and the bulk flow shear. The ion gyro-viscosity follows $\eta = \frac{R^2 \Omega}{4}$, where $R = \frac{M_i v_i}{QB}$ is the
421 gyroradius and $\Omega = \frac{QB}{M_i}$ is the gyrofrequency. Again, we compare relevant parameters
422 between Ganymede and Mercury to establish a limit for the Ganymedean FLR effect in Table
423 2. The Hermean gyro-viscosity coefficients are larger than the Ganymedean values by two
424 orders of magnitude. Meanwhile, the bulk flow shear has a much smaller difference but still
425 favoring Mercury by at least a factor of 2. The two parameters together suggest a
426 significantly more pronounced FLR effect at Mercury, supporting the earlier result from the
427 ion flow shear. However, the difference cannot be more precisely estimated without using the
428 full MHD-FLR theory.

429

430 We test the sensitivity of ion flow speed (v_i) and gyro-viscous coefficient (η) in Ganymede's
431 system by changing plasma ion mass (M_i), plasma temperature (T_i), and magnetic field
432 strength (B) by $\pm 50\%$ on both sides of the magnetopause (i.e., six total parameter changes).
433 The ion flow shear and gyro-viscous coefficient have proportional relations $v_i \propto \sqrt{\frac{T_i}{M_i}}$ and
434 $\eta \propto \frac{T_i}{B}$ respectively. Hence, ion temperature affects both parameters while ion mass and
435 magnetic field strength only affect ion flow speed and gyro-viscous coefficient respectively.
436 The single largest change occurs when the magnetic field strength is halved leading to a
437 doubling of gyro-viscous coefficient. As no parameter variation modifies v_i or η by an order
438 of magnitude, the conclusion on the comparative FLR effect between Ganymede and
439 Mercury is not sensitive to plasma/magnetic conditions near Ganymede's upstream
440 magnetopause.

441

442 **4. Discussion**

443 Under ideal MHD theory, Figure 2 shows that plasma and magnetic conditions along
444 Ganymede's magnetopause flanks ($|Y| > 2 R_G$) are favorable for linear K-H wave formation
445 at all latitudes for all Ganymede's positions in the Jovian plasma sheet. This result is obtained
446 using the inequality onset condition first established by Farrugia et al. (1998), also known as
447 the thin model. Gratton et al., (2004) have argued that this model correctly predicts K-H
448 instability only in limited cases where (1) the K-H wavevector is orthogonal to the adjacent
449 magnetic fields ($\mathbf{k} \cdot \mathbf{B} = 0$, or flute mode) and (2) the shear between adjacent magnetic fields
450 is small. The first condition is automatically satisfied since we do not restrict K-H
451 wavevector orientation in our analysis. Hence, for each K-H unstable point predicted by our
452 analytical model, the wavevector must be in flute mode as the orthogonal orientation
453 maximizes the difference between the two sides of the K-H instability onset inequality. The
454 second condition is also satisfied as the shear between Jovian and Ganymedeian magnetic
455 field are always within 10° of 180° in the analytical model (Kaweeyanun et al., 2020), so the
456 guide field effect is small and the magnetic configuration can be considered a variant of the
457 low-shear regime. Consequently, the thin model is a robust predictor for Ganymede's K-H
458 instability onset.

459

460 In Figure 4a, alignment of bulk and ion flow vorticities suggests that the FLR effect enhances
461 K-H instability growth at Ganymede's sub-Jovian magnetopause flank point ($X = 0, Z = 0$).
462 The asymmetry in growth is expected to be small but likely noticeable to future observations.
463 The Ganymedeian FLR effect is roughly quantified in Tables 1 and 2, which assume plasma
464 and magnetic conditions when Ganymede lies at the center of the Jovian plasma sheet

465 ($\phi = 248^\circ$). Nevertheless, the finding is applicable for all magnetopause flank latitudes
466 irrespective of Ganymede's position in the Jovian plasma sheet. This is because (1) the near-
467 magnetopause plasma-magnetic configuration remains sufficiently similar to Figure 4a for all
468 flank latitudes (Kaweeyanun et al., 2020) and (2) the comparative FLR effect is not sensitive
469 to changes in upstream Jovian plasma conditions.

470

471 Thus far, we have evaluated the onset of linear K-H instability and demonstrated that
472 subsequent growth will occur asymmetrically between magnetopause flanks. However, the
473 results provide little clarity on the expected abundance of nonlinear K-H vortices, which are
474 essential for cross-magnetopause energy transport. Given that transition between linear and
475 nonlinear K-H instability is not well-defined, there is no simple analytical solution for
476 determining K-H vortex onset. Nevertheless, it is still possible to establish a constrain on K-
477 H vortex growth near Ganymede using the fact that K-H instability does not occur in
478 isolation, but rather alongside other magnetopause processes, specifically magnetic
479 reconnection.

480

481 As discussed in Kaweeyanun et al., (2020), magnetic reconnection is expected to be very
482 common on Ganymede's magnetopause, which is also seen in global simulations (e.g., Jia,
483 Walker et al., 2010; Tóth et al., 2016; Zhou et al., 2020). Sufficiently frequent reconnection
484 events can suppress K-H vortex growth by rapidly altering plasma-magnetic conditions near
485 the magnetopause (Nakamura et al., 2020). The question of relative strengths between K-H
486 instability and reconnection has been investigated for planetary magnetopauses by Masters
487 (2018). However, the same method does not apply for Ganymede since the moon does not
488 interact with the solar wind.

489

490 Hence, we again consider the analogue case of Mercury's magnetopause, but this time when
491 the IMF is southward. In-situ observations from the MESSENGER mission find that only
492 11% of Mercury's K-H vortices occur under southward IMF (Liljeblad et al., 2014),
493 indicating a suppressive impact of Hermean reconnection on K-H instability growth.
494 Mercury's estimated reconnection electric field strength is $\sim 0.3\text{-}3$ mV/m (Gershman et al.,
495 2016), which is exceeded by Ganymede's typical values of $2\text{-}20$ mV/m (Kaweeyanun et al.,
496 2020; Zhou et al., 2020). As the two magnetospheres are similar in size, reconnection rates
497 can be compared directly via electric field strengths. Therefore, reconnection at Ganymede
498 occurs at higher rates and should have an even larger suppressive impact on K-H instability
499 growth than at Mercury, especially since the Jovian magnetic field is permanently southward
500 at Ganymede. Consequently, we expect few K-H vortices at Ganymede's magnetopause once
501 global reconnection is taken into account, and the latter interaction should be the dominant
502 mean of cross-magnetopause energy transport for Ganymede at all times.

503

504 The study of Ganymede's K-H instability growth has relied extensively on comparisons with
505 Mercury, whose system has very similar length scales. Despite this, a couple of factors may
506 hinder the effectiveness of our comparison. First, Figure 4b and other K-H instability studies
507 for Mercury (MHD-FLR or kinetic) assume the external IMF is strongly northward. In
508 reality, the IMF orientation continuously rotates between northward and southward
509 orientations. Figures 4a-4b are therefore not truly equivalent and the Ganymedean FLR effect
510 may be stronger than estimated from the ion flow shear. Second, K-H instability growth in its
511 linear phase depends on the K-H wavelengths in both MHD-FLR and kinetic studies (e.g.,
512 Sundberg et al., 2010; Nakamura et al., 2010). However, the wavelength is poorly

513 constrained for both Ganymede (1,050-1,400 km from Kivelson et al., 1998) and Mercury
514 (500-5,000 km from Nakamura et al., 2010). If the typical K-H wavelengths differ
515 significantly between the two bodies, then the divergent linear growth rate may exaggerate or
516 minimize comparative strength of the FLR effect predicted in Section 3.

517

518 The analytical model assumes that plasma inside Ganymede's magnetopause is completely
519 stagnant and very low in temperature. However, magnetic reconnection is also expected in
520 Ganymede's downstream magnetotail due to Dungey-like plasma convection. Numerical
521 simulations suggest that downstream reconnection generates bulk plasma flow speed
522 $v_G = 20 - 50$ km/s along the Ganymede-side magnetopause flank, in direction antiparallel
523 to the Jovian-side flow (e.g., Jia et al., 2009). Galileo observations also indicate that the
524 Ganymedean plasma may be warmer than $T_{i,G} = 1$ eV (Collinson et al., 2018). Incorporating
525 finite v_G and a larger $T_{i,G} < T_{i,J}$ will not significantly change the size of K-H unstable area,
526 nor the orders of magnitude for ion flow speed or gyro-viscous coefficients. Hence, the
527 uncertainties in Ganymedean plasma properties would not change the main conclusions
528 drawn.

529

530 Our discussion does not consider impacts of adjacent magnetic field realignments in response
531 to initial K-H instability growth, which can introduce a stabilizing guide effect, or other
532 disruptive factors such as pressure rarefaction regions near the magnetopause (Miura, 1995)
533 and ion cyclotron waves (Volwerk et al., 1999; Volwerk et al., 2013). However, these factors
534 are potential subjects for future research on K-H instability growth along Ganymede's
535 upstream magnetopause.

536

537 **5. Conclusion**

538 Dynamics within Ganymede's unique magnetosphere are thought to be driven primarily by
539 energy-transfer interactions on the moon's upstream magnetopause. One such interaction is
540 the Kelvin-Helmholtz (K-H) instability particularly during its turbulent nonlinear vortex
541 phase. This paper details the first assessment of K-H instability growth on Ganymede's
542 upstream magnetopause, using a previously established analytical model to capture the
543 plasma and magnetic conditions near the boundary (Kaweeyanun et al., 2020).

544

545 In a two-part assessment, we first evaluate the K-H instability onset condition to reveal the
546 extent of global-scale linear K-H wave growth on the Ganymedean magnetopause.
547 Conditions along the magnetopause flank regions are found to be favorable for K-H
548 instability. The K-H waves are expected to be more prevalent when Ganymede is at the
549 center of the Jovian plasma sheet, which is opposite from global-scale magnetic reconnection
550 which favors conditions when Ganymede is at its highest/lowest points relative to the plasma
551 sheet.

552

553 Then, we establish a schematic picture of the kinetic finite Larmor radius (FLR) effect that is
554 responsible for asymmetric K-H instability growth between Ganymede's two magnetopause
555 flanks. The principle of bulk-ion vorticity alignment predicts growth enhancement on the
556 sub-Jovian flank. A subsequent study of local ion flow shear and gyro-viscosity, aided by
557 comparisons with well-observed K-H instability phenomena at Mercury, suggests that the
558 enhancement is likely small but noticeable to future prolonged observations.

559

560 Existing information on linear K-H instability onset and the FLR effect does not yield a clear
561 forecast for nonlinear K-H vortex growth on Ganymede's magnetopause flanks. However, a
562 constrain on K-H vortices is possible by determining relative strengths between K-H

563 instability and concurring global-scale magnetic reconnection. Using Mercury's
564 magnetopause as an analogue, it can be shown that Ganymede's frequent reconnection should
565 have a strong suppressive effect on K-H vortex growth (Jia, Walker et al., 2010; Kaweeyanun
566 et al., 2020; Zhou et al., 2020). Therefore, magnetic reconnection is likely the dominant
567 energy-transfer interaction on Ganymede's upstream magnetopause.

568

569 Our results remain largely qualitative due to the approximative models used for Ganymede's
570 magnetopause and the FLR effect. Nevertheless, the analytical method captures the primary
571 physics of K-H instability growth and using more detailed descriptions should not impact the
572 main conclusions drawn, especially given the expected dominance of magnetic reconnection.
573 Our findings lay groundwork for future studies of global-scale plasma convection within
574 Ganymede's magnetosphere, and can also help inform the planning for the upcoming JUpiter
575 ICy moon Explorer (JUICE) mission.

576

577 **Acknowledgements**

578 NK is supported by a Royal Society PhD Studentship, and AM is supported by a Royal
579 Society University Research Fellowship. Derived data in Figures 1-3 and 5-6 is available in
580 the Imperial College High Performance Computing Service Data Repository (Kaweeyanun,
581 2020b).

582 **Reference**

583 Anderson, J. D., Lau, E. L., Sjogren, W. L., Schubert, G., & Moore, W. B. (1996).
584 Gravitational constraints on the internal structure of Ganymede. *Nature*, 384 (6609), 541–
585 543. <https://doi.org/10.1038/384541a0>

586

587 Bagenal, F., Wilson, R. J., Siler, S., Paterson, W. R., & Kurth, W. S. (2016). Survey of
588 Galileo plasma observations in Jupiter's plasma sheet. *Journal of Geophysical Research:*
589 *Planets*, 121 (5), 871– 894. <https://doi.org/10.1002/2016JE005009>

590

591 Boardsen, S. A., Sundberg, T., Slavin, J. A., Anderson, B. J., Korth, H., Solomon, S. C., &
592 Blomberg, L. G. (2010). Observations of Kelvin-Helmholtz waves along the dusk-side
593 boundary of Mercury's magnetosphere during Messenger's third flyby. *Geophysical*
594 *Research Letters*, 37 (12). <https://doi.org/10.1029/2010GL043606>

595

596 Chaston, C., Wilber, M., Mozer, F., Fujimoto, M., Goldstein, M., Acuña, M., . . . Fazakerley,
597 A. (2007, 11). Mode conversion and anomalous transport in Kelvin-Helmholtz vortices and
598 kinetic Alfvén waves at the Earth's magnetopause. *Physical review letters*, 99, 175004.
599 <http://doi.org/10.1103/PhysRevLett.99.175004>

600

601 Chen, Q., Otto, A., & Lee, L. C. (1997). Tearing instability, Kelvin-Helmholtz instability,
602 and magnetic reconnection. *Journal of Geophysical Research: Space Physics*, 102 (A1), 151–
603 161. <https://doi.org/10.1029/96JA03144>

604

605 Collinson, G., Paterson, W. R., Bard, C., Dorelli, J., Glocer, A., Sarantos, M., & Wilson, R.
606 (2018). New results from Galileo's first flyby of Ganymede: Reconnection-driven flows at
607 the low-latitude magnetopause boundary, crossing the cusp, and icy ionospheric escape.
608 *Geophysical Research Letters*, 45(8), 3382–3392. <https://doi.org/10.1002/2017GL075487>

609

610 Delamere, P. A., Wilson, R. J., Eriksson, S., & Bagenal, F. (2013, 2020/07/08). Magnetic
611 signatures of kelvin-helmholtz vortices on Saturn's magnetopause: Global survey. *Journal of*
612 *Geophysical Research: Space Physics*, 118 (1), 393–404.
613 <https://doi.org/10.1029/2012JA018197>

614

615 Desroche, M., Bagenal, F., Delamere, P. A., & Erkaev, N. (2012). Conditions at the expanded
616 Jovian magnetopause and implications for the solar wind interaction. *Journal of Geophysical*
617 *Research: Space Physics*, 117(A7). <https://doi.org/10.1029/2012JA017621>

618

619 Dungey, J. (1955). Electrodynamics of the outer atmosphere. In *Physics of the ionosphere*,
620 report of the conference held at the cavendish laboratory. Cambridge: The Physical Society.

621

622 Eastwood, J. P., Hietala, H., Toth, G., Phan, T. D., & Fujimoto, M. (2015). What controls the
623 structure and dynamics of Earth's magnetosphere? *Space Science Reviews*, 188 (1), 251–
624 286. <https://doi.org/10.1007/s11214-014-0050-x>

625

626 Eviatar, A., M. Vasyliūnas, V., & A. Gurnett, D. (2001). The ionosphere of Ganymede.
627 *Planetary and Space Science*, 49(3), 327–336. [https://doi.org/10.1016/S0032-0633\(00\)00154-](https://doi.org/10.1016/S0032-0633(00)00154-9)
628 [9](https://doi.org/10.1016/S0032-0633(00)00154-9)

629

630 Fairfield, D. H., Otto, A., Mukai, T., Kokubun, S., Lepping, R. P., Steinberg, J. T., ...
631 Yamamoto, T. (2000). Geotail observations of the Kelvin-Helmholtz instability at the
632 equatorial magnetotail boundary for parallel northward fields. *Journal of Geophysical*
633 *Research: Space Physics*, 105 (A9), 21159–21173. <https://doi.org/10.1029/1999JA000316>

634

635 Farrugia, C. J., Gratton, F. T., Bender, L., Biernat, H. K., Erkaev, N. V., Quinn, J. M., ...
636 Dennisenko, V. (1998). Charts of joint Kelvin-Helmholtz and Rayleigh-Taylor instabilities at
637 the dayside magnetopause for strongly northward interplanetary magnetic field. *Journal of*
638 *Geophysical Research: Space Physics*, 103 (A4), 6703– 6727.
639 <https://doi.org/10.1029/97JA03248>

640

641 Frank, L. A., Paterson, W. R., Ackerson, K. L., & Bolton, S. J. (1997). Outflow of hydrogen
642 ions from Ganymede. *Geophysical Research Letters*, 24 (17), 2151–2154.

643 <https://doi.org/10.1029/97GL01744>

644

645 Gershman, D. J., Dorelli, J. C., DiBraccio, G. A., Raines, J. M., Slavin, J. A., Poh, G., &
646 Zurbuchen, T. H. (2016). Ion-scale structure in Mercury's magnetopause reconnection
647 diffusion region. *Geophysical Research Letters*, 43 (12), 5935–5942.

648 <https://doi.org/10.1002/2016GL069163>

649

650 Glassmeier, K.-H., & Espley, J. (2006). ULF waves in planetary magnetospheres (Vol. 169;
651 K. Takahashi, Ed.). American Geophysical Union <https://doi.org/10.1029/169GM22>

652

653 Grasset, O., Dougherty, M. K., Coustenis, A., Bunce, E., Erd, C., Titov, D. V., ... Van Hoolst,
654 T. (2013). JUPiter ICy moons Explorer (JUICE): An ESA mission to orbit Ganymede and to
655 characterise the Jupiter system. *Planetary and Space Science*, 78, 1–21.

656 <http://doi.org/10.1016/j.pss.2012.12.002>

657

658 Gratton, F. T., Bender, L., Farrugia, C. J., & Gnani, G. (2004). Concerning a problem on the
659 Kelvin-Helmholtz stability of the thin magnetopause. *Journal of Geophysical Research:*
660 *Space Physics*, 109(A4). <https://doi.org/10.1029/2003JA010146>

661

662 Gurnett, D. A., Kurth, W. S., Roux, A., Bolton, S. J., & Kennel, C. F. (1996). Evidence for a
663 magnetosphere at Ganymede from plasma-wave observations by the Galileo spacecraft.
664 Nature, 384 (6609), 535–537. <https://doi.org/10.1038/384535a0>

665

666 Hasegawa, H., Fujimoto, M., Phan, T. D., Rème, H., Balogh, A., Dunlop, M. W., ...
667 TanDokoro, R. (2004). Transport of solar wind into Earth's magnetosphere through rolled-up
668 Kelvin–Helmholtz vortices. Nature, 430(7001), 755–758.
669 <https://doi.org/10.1038/nature02799>

670

671 Huba, J. (1996). The Kelvin-Helmholtz instability: Finite Larmor radius
672 magnetohydrodynamics. Geophysical Research Letters – Geophysical Research Letters, 23.
673 <http://doi.org/10.1029/96GL02767>

674

675 Hwang, K. J., Kuznetsova, M. M., Sahraoui, F., Goldstein, M. L., Lee, E., & Parks, G. K.
676 (2011). Kelvin-Helmholtz waves under southward interplanetary magnetic field. Journal of
677 Geophysical Research: Space Physics, 116 (A8). <https://doi.org/10.1029/2011JA016596>

678

679 Jia, X., Kivelson, M. G., Khurana, K. K., & Walker, R. J. (2010). Magnetic fields of the
680 satellites of Jupiter and Saturn. Space Science Reviews, 152(1), 271–305.
681 <https://doi.org/10.1007/s11214-009-9507-8>

682

683 Jia, X., Walker, R. J., Kivelson, M. G., Khurana, K. K., & Linker, J. A. (2008). Three-
684 dimensional MHD simulations of Ganymede's magnetosphere. *Journal of Geophysical*
685 *Research: Space Physics*, 113(A6). <https://doi.org/10.1029/2007JA012748>

686

687 Jia, X., Walker, R. J., Kivelson, M. G., Khurana, K. K., & Linker, J. A. (2009). Properties of
688 Ganymede's magnetosphere inferred from improved three-dimensional MHD simulations.
689 *Journal of Geophysical Research: Space Physics*, 114 (A9).
690 <https://doi.org/10.1029/2009JA014375>

691

692 Jia, X., R. J. Walker, M. G. Kivelson, K. K. Khurana and J. A. Linker (2010). Dynamics of
693 Ganymede's magnetopause: Intermittent reconnection under steady external
694 conditions, *Journal of Geophysical Research – Space Physics*, Vol. 115, A12202,
695 <http://doi.org/10.1029/2010JA015771>

696

697 Kavosi, S., & Raeder, J. (2015). Ubiquity of Kelvin–Helmholtz waves at Earth's
698 magnetopause. *Nature Communications*, 6 (1), 7019. <https://doi.org/10.1038/ncomms8019>

699

700 Kaweeyanun, N. (2020b). (Supplementary Data) Analytical assessment of Kelvin-Helmholtz
701 instability growth at Ganymede's upstream magnetopause. Version 1.0. Imperial College
702 High Performance Computing Service Data Repository.
703 <http://www.doi.org/10.14469/hpc/7399>.

704

705 Kaweeyanun, N., Masters, A., & Jia, X. (2020). Favorable conditions for magnetic
706 reconnection at Ganymede's upstream magnetopause. *Geophysical Research Letters*, 47 (6),
707 e2019GL086228. <https://doi.org/10.1029/2019GL086228>

708

709 Khurana, K. K. (1997). Euler potential models of Jupiter's magnetospheric field. *Journal of*
710 *Geophysical Research: Space Physics*, 102(A6), 11295–11306.
711 <https://doi.org/10.1029/97JA00563>

712

713 Kivelson, M., Bagenal, F., Kurth, W., Neubauer, F., Paranicas, C., & Saur, J. (2004).
714 *Magnetospheric interactions with satellites* (Vol. 1; F. Bagenal, T. Dowling, & W.
715 McKinnon, Eds.). Cambridge University Press.

716

717 Kivelson, M. G., Khurana, K. K., Russell, C. T., Walker, R. J., Warnecke, J., Coroniti, F. V.,
718 ... Schubert, G. (1996). Discovery of Ganymede's magnetic field by the Galileo spacecraft.
719 *Nature*, 384 (6609), 537–541. <https://doi.org/10.1038/384537a0>

720

721 Kivelson, M. G., Khurana, K. K., & Volwerk, M. (2002). The permanent and inductive
722 magnetic moments of Ganymede. *Icarus*, 157 (2), 507–522.
723 <https://doi.org/10.1006/icar.2002.6834>

724

725 Kivelson, M. G., Warnecke, J., Bennett, L., Joy, S., Khurana, K. K., Linker, J. A., . . .

726 Polanskey, C. (1998). Ganymede's magnetosphere: Magnetometer overview. *Journal of*

727 *Geophysical Research: Planets*, 103 (E9), 19963–19972. <https://doi.org/10.1029/98JE00227>

728

729 Liljeblad, E., Sundberg, T., Karlsson, T., & Kullen, A. (2014). Statistical investigation of

730 Kelvin-Helmholtz waves at the magnetopause of Mercury. *Journal of Geophysical Research:*

731 *Space Physics*, 119(12), 9670– 9683. <https://doi.org/10.1002/2014JA020614>

732

733 Masters, A. (2017). Model-based assessments of magnetic re-connection and Kelvin-

734 Helmholtz instability at Jupiter's magnetopause. *Journal of Geophysical Research: Space*

735 *Physics*, 122 (11), 11,154– 11,174. <https://doi.org/10.1002/2017JA024736>

736

737 Masters, A., Achilleos, N., Bertucci, C., Dougherty, M. K., Kanani, S. J., Arridge, C. S., ...

738 Coates, A. J. (2009). Surface waves on Saturn's dawn flank magnetopause driven by the

739 Kelvin-Helmholtz instability. *Planetary and Space Science*, 57 (14), 1769–1778.

740 <https://doi.org/10.1016/j.pss.2009.02.010>

741

742 Masters, A., Achilleos, N., Kivelson, M. G., Sergis, N., Dougherty, M. K., Thomsen, M. F., .

743 . . Coates, A. J. (2010). Cassini observations of a Kelvin-Helmholtz vortex in Saturn's outer

744 magnetosphere. Journal of Geophysical Research: Space Physics, 115(A7).

745 <https://doi.org/10.1029/2010JA015351>

746

747 Matsumoto, Y., & Hoshino, M. (2004). Onset of turbulence induced by a Kelvin-Helmholtz

748 vortex. Geophysical Research Letters, 31(2). <https://doi.org/10.1029/2003GL018195>

749

750 Matsumoto, Y., & Hoshino, M. (2006). Turbulent mixing and transport of collisionless

751 plasmas across a stratified velocity shear layer. Journal of Geophysical Research: Space

752 Physics, 111(A5). <https://doi.org/10.1029/2004JA010988>

753

754 Miura, A. (1982). Nonlinear evolution of the magnetohydrodynamic Kelvin-Helmholtz

755 instability. Phys. Rev. Lett., 49, 779–782. <http://doi.org/10.1103/PhysRevLett.49.779>

756

757 Miura, A. (1995). Dependence of the magnetopause Kelvin-Helmholtz instability on the

758 orientation of the magnetosheath magnetic field. Geophysical Research Letters, 22(21),

759 2993–2996. <https://doi.org/10.1029/95GL02793>

760

761 Nagano, H. (1978). Effect of finite ion Larmor radius on the Kelvin–Helmholtz instability. ,

762 20(2), 149-160. <http://doi.org/10.1017/S0022377800021450>

763

764 Nagano, H. (1979). Effect of finite ion Larmor radius on the Kelvin-Helmholtz instability of
765 the magnetopause. *Planetary and Space Science*, 27(6), 881–884.

766 [https://doi.org/10.1016/0032-0633\(79\)90013-8](https://doi.org/10.1016/0032-0633(79)90013-8)

767

768 Nakamura, T., Fujimoto, M., & Otto, A. (2008). Structure of an MHD-scale Kelvin-
769 Helmholtz vortex: Two-dimensional two-fluid simulations including finite electron inertial
770 effects. *Journal of Geophysical Research: Space Physics*, 113 (A9).

771 <http://doi.org/10.1029/2007JA012803>

772

773 Nakamura, T., Hayashi, D., Fujimoto, M., & Shinohara, I. (2004). Decay of MHD-scale
774 Kelvin-Helmholtz vortices mediated by parasitic electron dynamics. *Physical Review Letters*,
775 92, 145001. <http://doi.org/10.1103/Phys-RevLett.92.145001>

776

777 Nakamura, T., Hasegawa, H., & Shinohara, I. (2010). Kinetic effects on the Kelvin-
778 Helmholtz instability in ion-to-magnetohydrodynamic scale transverse velocity shear layers:
779 Particle simulations. *Physics of Plasmas*, 17. <http://doi.org/10.1063/1.3385445>

780

781 Nakamura, T. K. M., Plaschke, F., Hasegawa, H., Liu, Y. H., Hwang, K. J., Blasl, K. A., &
782 Nakamura, R. (2020). Decay of Kelvin-Helmholtz vortices at the Earth's magnetopause
783 under pure southward IMF conditions. *Geophysical Research Letters*, 47 (13),

784 e2020GL087574. <https://doi.org/10.1029/2020GL087574>

785

786 Neubauer, F. (1998). The sub-Alfvénic interaction of the Galilean satellites with the Jovian
787 magnetosphere (Vol. 103). <http://doi.org/10.1029/97JE03370>

788

789 Neubauer, F. M. (1990). Satellite plasma interactions. *Advances in Space Research*, 10, 25–
790 38. [http://doi.org/10.1016/0273-1177\(90\)90083-C](http://doi.org/10.1016/0273-1177(90)90083-C)

791

792 Nykyri, K., & Otto, A. (2001). Plasma transport at the magnetospheric boundary due to
793 reconnection in Kelvin-Helmholtz vortices. *Geophysical Research Letters*, 28(18), 3565–
794 3568. <https://doi.org/10.1029/2001GL013239>

795

796 Owen, C., Taylor, M., Krauklis, I., Fazakerley, A., Dunlop, M., & Bosqued, J. (2004).
797 Cluster observations of surface waves on the dawn flank magnetopause. *Annales*
798 *Geophysicae*, 22(3). pp. 971-983. ISSN 09927689, 22. [http://doi.org/10.5194/angeo-22-971-](http://doi.org/10.5194/angeo-22-971-2004)
799 [2004](http://doi.org/10.5194/angeo-22-971-2004)

800

801 Paral, J., & Rankin, R. (2013). Dawn–dusk asymmetry in the Kelvin–Helmholtz instability at
802 Mercury. *Nature Communications*, 4 (1), 1645. <https://doi.org/10.1038/ncomms2676>

803

804 Schubert, G., Zhang, K., Kivelson, M. G., & Anderson, J. D. (1996). The magnetic field and
805 internal structure of Ganymede. *Nature*, 384 (6609), 544–545.

806 <https://doi.org/10.1038/384544a0>

807

808 Slavin, J., Acuña, M., Anderson, B., Baker, D., Benna, M., Gloeckler, G., . . . Zurbuchen, T.

809 (2008). Mercury's magnetosphere after Messenger's first flyby. *Science* (New York, N.Y.),

810 321, 85–9. <http://doi.org/10.1126/science.1159040>

811

812 Southwood, D. J. (1968). The hydromagnetic stability of the magnetospheric boundary.

813 *Planetary and Space Science*, 16, 587-605.

814

815 Southwood, D. J. (1979). Magnetopause kelvin-helmholtz instability. In *Proceedings of*

816 *magnetospheric boundary layers conference*. Noordwijk, the Netherlands.

817

818 Sundberg, T., Boardsen, S. A., Slavin, J. A., Anderson, B. J., Korth, H., Zurbuchen, T. H., . . .

819 Solomon, S. C. (2012). Mercury orbital observations of large-amplitude Kelvin-Helmholtz

820 waves at Mercury's magnetopause. *Journal of Geophysical Research: Space Physics*,

821 117(A4). <https://doi.org/10.1029/2011JA017268>

822

823 Sundberg, T., Boardsen, S. A., Slavin, J. A., Blomberg, L. G., & Korth,
824 H. (2010). The Kelvin–Helmholtz instability at Mercury: An assessment. *Planetary and*
825 *Space Science*, 58(11), 1434–1441. <https://doi.org/10.1016/j.pss.2010.06.008>

826

827 Thomas, V. A., & Winske, D. (1993, 2020/06/18). Kinetic simulations of the Kelvin-
828 Helmholtz instability at the magnetopause. *Journal of Geophysical Research: Space Physics*,
829 98(A7), 11425–11438. <https://doi.org/10.1029/93JA00604>

830

831 Tóth, G., Jia, X., Markidis, S., Peng, I. B., Chen, Y., Daldorff, L. K. S., . . . Dorelli, J. C.
832 (2016). Extended magnetohydrodynamics with embedded particle-in-cell simulation of
833 Ganymede’s magnetosphere. *Journal of Geophysical Research: Space Physics*, 121(2), 1273–
834 1293. <https://doi.org/10.1002/2015JA021997>

835

836 Umeda, T., Yamauchi, N., Wada, Y., & Ueno, S. (2016). Evaluating gyro-viscosity in the
837 Kelvin-Helmholtz instability by kinetic simulations. *Physics of Plasmas*, 23 (5), 054506.
838 <https://doi.org/10.1063/1.4952632>

839

840 Volwerk, M., Jia, X., Paranicas, C., Kurth, W. S., Kivelson, M. G., & Khurana, K. K. (2013).
841 Ulf waves in Ganymede’s upstream magnetosphere. *Annales Geophysicae*, 31(1), 45–59.
842 <https://doi.org/10.5194/angeo-31-45-2013>

843

844 Volwerk, M., Kivelson, M. G., Khurana, K. K., & McPherron, R. L. (1999). Probing
845 Ganymede's magnetosphere with field line resonances. *Journal of Geophysical Research:*
846 *Space Physics*, 104(A7), 14729– 14738. <https://doi.org/10.1029/1999JA900161>

847

848 Williams, D. J., Mauk, B., & McEntire, R. W. (1997). Trapped electrons in Ganymede's
849 magnetic field. *Geophysical Research Letters*, 24(23), 2953–2956.
850 <https://doi.org/10.1029/97GL03003>

851

852 Williams, D. J., Mauk, B. H., McEntire, R. W., Roelof, E. C., Armstrong, T. P., Wilken, B., .
853 . . Murphy, N. (1997). Energetic particle signatures at Ganymede: Implications for
854 Ganymede's magnetic field. *Geophysical Research Letters*, 24(17), 2163–2166.
855 <https://doi.org/10.1029/97GL01931>

856

857 Yan, G. Q., Mozer, F. S., Shen, C., Chen, T., Parks, G. K., Cai, C. L., & McFadden, J. P.
858 (2014, 2021/03/03). Kelvin-Helmholtz vortices observed by THEMIS at the duskside of the
859 magnetopause under southward interplanetary magnetic field. *Geophysical Research Letters*,
860 41 (13), 4427– 4434. <https://doi.org/10.1002/2014GL060589>

861

862 Zhou, H., Tóth, G., Jia, X., & Chen, Y. (2020). Reconnection-driven dynamics at
863 Ganymede's upstream magnetosphere: 3d global hall MHD and MHD-EPIC simulations.

864 Journal of Geophysical Research: Space Physics, n/a (n/a), e2020JA028162.

865 <https://doi.org/10.1029/2020JA028162>

866 *Table 1: Local ion flow shear across a magnetopause flank for Ganymede and Mercury*

	Ganymede		Mercury (perihelion)		Mercury (aphelion)	
	J	G	MSH	MSP	MSH	MSP
T_i (10^6 K)	0.70 ^a	0.01 ^b	8 ^d	23 ^d	6 ^d	23 ^d
M (amu)	14 ^a	16 ^{b,c}	1	1	1	1
v_i (km/s)	28.6	3.46	371	630	322	630
$v_{i,sh}$ (km/s)	+25.2		-258		-308	

867 Data Source: (a) Kivelson et al., 2004; (b) Jia et al., 2008; (c) Eviatar et al., 2001; (d) Sundberg et al., 2010

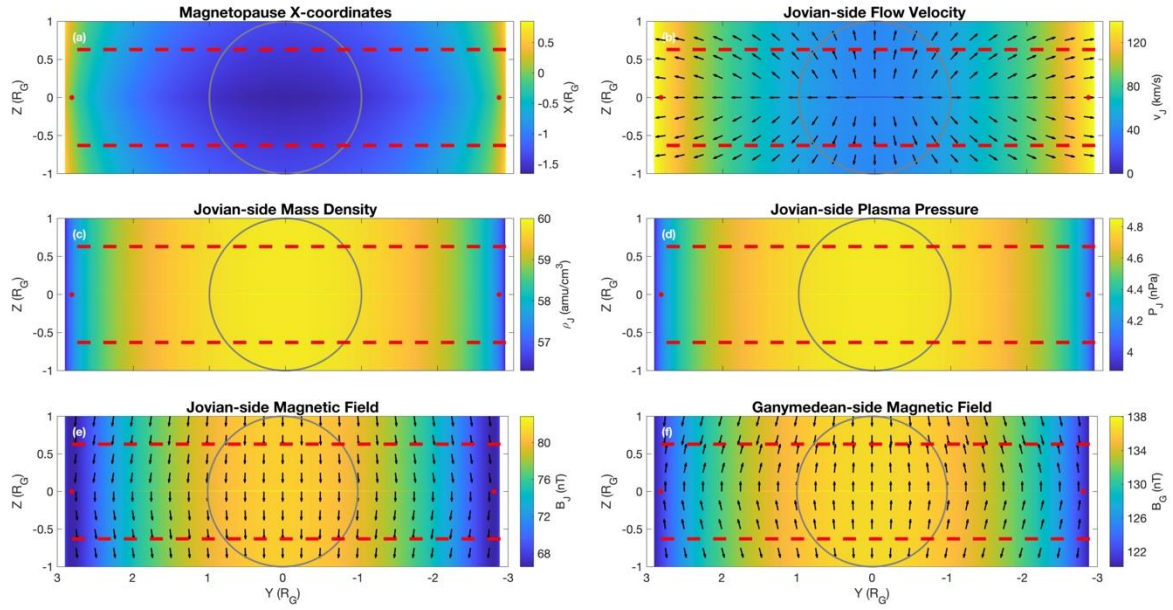
868 Notes: J = Jupiter, G = Ganymede, MSH = magnetosheath, MSP = magnetosphere. Plasmas
 869 near Mercury's magnetopause are assumed to be protons only. Ion flow shear is highlighted
 870 in bold.

871 *Table 2: Gyro-viscous coefficients and bulk flow shear near a magnetopause flank for*
 872 *Ganymede and Mercury*

	Ganymede		Mercury (perihelion)		Mercury (aphelion)	
	J	G	MSH	MSP	MSH	MSP
B (nT)	67 ^e	122 ^e	46 ^d	15 ^d	21 ^d	15 ^d
R (km)	62.5	4.74	80.8	420	153	420
Ω (s ⁻¹)	0.46	0.73	4.60	1.50	2.10	1.50
η (10 ⁸ m ² /s)	4.48	0.04	75.0	661	123	661
$\Sigma \eta$ (10 ⁸ m ² /s)	4.52		736		784	
v_{sh} (km/s)	~140^b		~400^d		~400^d	

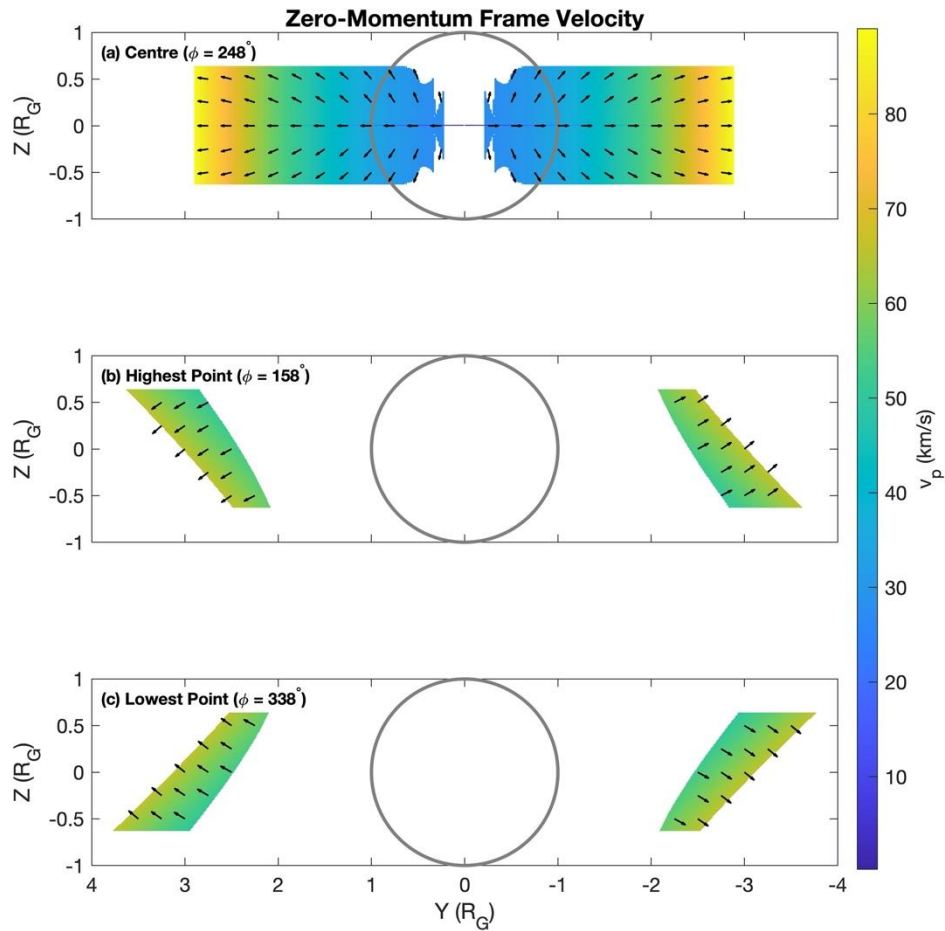
873 Data Source: (d) Sundberg et al., 2010; (e) Figures 1e-1f at (X = 0, Z = 0)

874 Notes: Column header definitions are the same as in Table 1. All plasmas are assumed to be
 875 singly charged. Gyro-viscous coefficients are calculated using T_i and M data in Table 1. Sum
 876 of gyro-viscous coefficients and bulk flow shears are highlighted in bold.



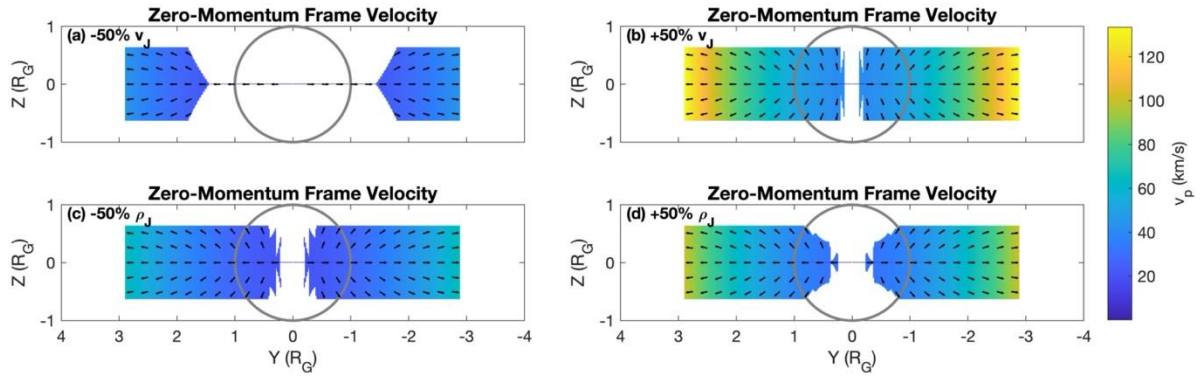
877

878 Figure 1: Near-magnetopause plasma and magnetic conditions computed by a steady-state
 879 analytical model of Ganymede's magnetopause (adapted from Kaweeyanun et al., 2020).
 880 Parameters shown are (a) magnetopause X-coordinates, (b) Jovian-side bulk flow velocity,
 881 (c) Jovian-side plasma mass density, (d) Jovian-side pressure, (e) Jovian-side magnetic field,
 882 and (f) Ganymede-side magnetic field. In each subplot, the closed-field region between
 883 two red dashed lines while the two red dots denote equatorial flank points later used for gyro-
 884 viscous coefficient calculations in Section 3. Ganymede is outlined in grey.



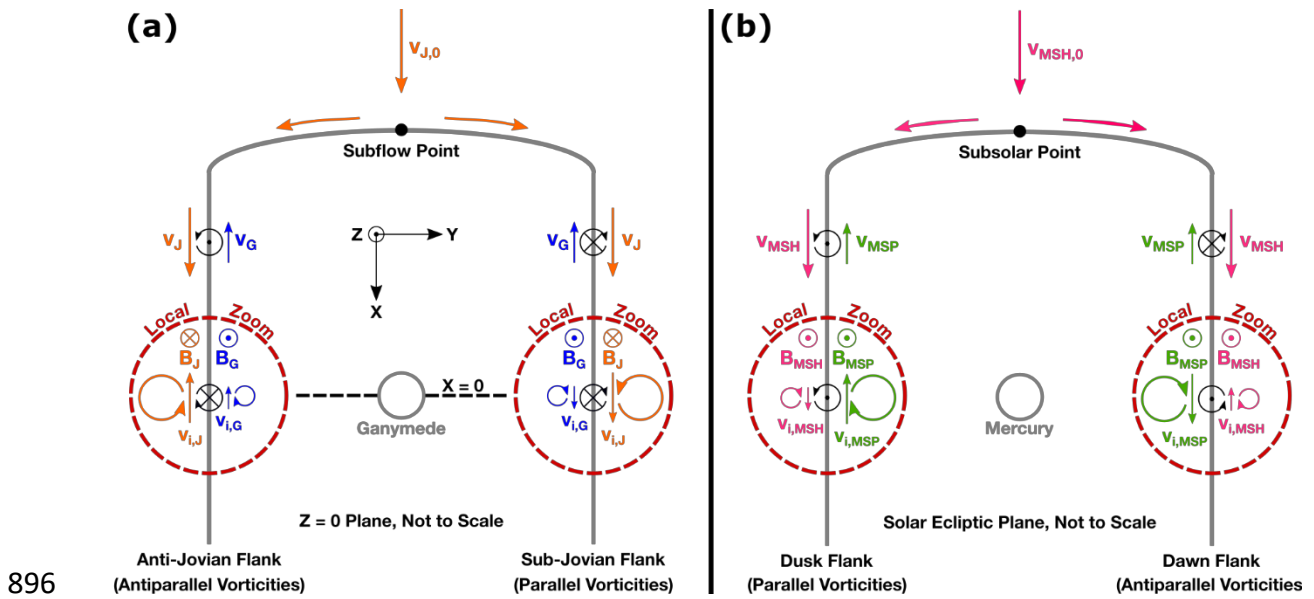
885

886 Figure 2: K-H instability onset assessment when Ganymede lies at (a) center of Jovian
 887 plasma sheet and (b/c) highest/lowest points relative to the plasma sheet. K-H unstable
 888 locations correspond to colored regions. The shared color bar denotes the speed, and the
 889 normalized arrows denotes the direction, of zero-momentum frame velocity for the linear K-
 890 H wave once formed. Ganymede is outlined in grey.



891

892 Figure 3: K-H instability onset assessment when Ganymede lies at center of the Jovian
 893 plasma sheet ($\phi = 258^\circ$), but with Jovian-side plasma conditions varied to simulate temporal
 894 effects. Parameters considered are (a) -50% bulk flow speed, (b) +50% bulk flow speed, (c) -
 895 50% mass density, and (d) +50% mass density. The format is the same as Figure 2.



897 Figure 4: Schematic diagrams for K-H instability growth on the magnetopause flanks of (a)
 898 Ganymede and (b) Mercury in their respective equatorial planes. In each diagram, bulk
 899 plasma motions (colored straight arrows) either side of the magnetopause produce bulk
 900 vorticities (black circular arrows) in opposite direction between the two flanks. Local ion
 901 motions are shown inside zoom windows (red dashed lines). Ions gyrate (colored circular
 902 arrows) around near-magnetopause magnetic fields (directed into or out of page) following
 903 the left-hand rule. Subsequent local ion flows (straight colored arrows) produce ion vorticities
 904 (black circular arrows) in the same direction on both flanks. Both diagrams are not to scale.